Polymer Chemistry

Role of chain architecture on the solution phase assembly and thermoreversibility of aqueous PNIPAM/silyl methacrylate copolymers

Journal:	*Polymer Chemistry*
Manuscript ID	PY-ART-02-2022-000254.R1
Article Type:	Paper
Date Submitted by the Author:	11-Apr-2022
Complete List of Authors:	Linn, Jason; University of Minnesota Twin Cities, Chemical Engineering and Materials Science Liberman, Lucy; University of Minnesota Twin Cities, Chemical Engineering and Materials Science Neal, Christopher Andrew Parker; University of Minnesota Twin Cities, Chemical Engineering and Materials Science Calabrese, Michelle; University of Minnesota System, Chemical Engineering and Materials Science

Journal Name

ARTICLE TYPE

Cite this: DOI: 00.0000/xxxxxxxxxx

Role of chain architecture on the solution phase assembly and thermoreversibility of aqueous PNIPAM/silyl methacrylate copolymers†

Jason D. Linn, Lucy Liberman, Christopher A. P. Neal, and Michelle A. Calabrese*

Received Date
Accepted Date

DOI: 00.0000/xxxxxxxxxx

Stimuli-responsive polymers functionalized with reactive inorganic groups enable creation of macromolecular structures such as hydrogels, micelles, and coatings that demonstrate smart behavior. Prior studies using poly(N-isopropyl acrylamide-co-3-(trimethoxysilyl)propyl methacrylate) (P(NIPAM-co-TMA)) have stabilized micelles and produced functional nanoscale coatings; however, such systems show limited responsiveness over multiple thermal cycles. Here, polymer architecture and TMA content are connected to the aqueous self-assembly, optical response, and thermo-reversibility of two distinct types of PNIPAM/TMA copolymers: random P(NIPAM-co-TMA), and a 'blocky-functionalized' copolymer where TMA is localized to one portion of the chain, P(NIPAM-b-NIPAM-co-TMA). Aqueous solution behavior characterized via cloud point testing (CPT), dynamic light scattering (DLS), and variable-temperature nuclear magnetic resonance spectroscopy (NMR) demonstrates that thermoresponsiveness and thermoreversibility over multiple cycles is a strong function of polymer configuration and TMA content. Despite low TMA content ($\leq$2% mol), blocky-functionalized copolymers assemble into small, well-ordered structures above the cloud point that lead to distinct transmittance behaviors and stimuli-responsiveness over multiple cycles. Conversely, random copolymers form disordered aggregates at elevated temperatures, and only exhibit thermoreversibility at negligible TMA fractions (0.5% mol); higher TMA content leads to irreversible structure formation. This understanding of the architectural and assembly effects on the thermal cyclability of aqueous PNIPAM-co-TMA can be used to improve the scalability of responsive polymer applications requiring thermoreversible behavior, including sensing, separations, and functional coatings.

1 Introduction

Polymers containing inorganic silicon functionalities, such as alkoxysilanes, are a versatile class of materials that can be used to develop films,[1] gels,[2] biomaterials,[3] and particles[4] with controlled properties. The inorganic functionalities can be used to graft polymers onto surfaces[5] and create intermolecular crosslinks,[6] enabling the formation of covalently-bonded, class II hybrid materials and self-assembled particles. Of particular interest is combining inorganic functionalities with responsive polymers, which can undergo dramatic changes in conformation in response to a variety of stimuli, including thermal,[7,8] pH,[9–14] electrical,[15–17] optical,[18,19] and biological stimuli,[20,21] among others.[22] Because of these properties, responsive polymers with inorganic functionalities have been used to develop systems for a wide range of applications including drug delivery,[2,13,23–25] sensing,[1,26,27] and controlled nano-assemblies.[4,28]

Poly(*N*-isopropyl acrylamide) (PNIPAM) is a thermoresponsive polymer of strong interest for incorporating inorganic functionalities, as the polymer has been studied extensively for a range of applications, including drug delivery[25,29,30] and sensing.[31–33] Aqueous PNIPAM solutions have a lower critical solution temperature (LCST) at biologically-relevant temperatures (typically near 35 °C), where the conformation of the chains dramatically changes, leading to phase separation.[34] Below the LCST, the polymer is miscible and the water forms hydrogen bonds with the amide protons. Above the LCST, the entropic drive for disordered phase separation dominates, causing the polymer to become immiscible, expel solvent, and collapse into globules.[35] The solutions become opaque due to the globules aggregating and scattering light.[34,36] Altering the solution composition and introducing comonomers can change the balance of enthalpic and entropic contributions that lead to phase separation, impacting the solution behavior of PNIPAM;[37–39] thus, these highly tunable systems can be adapted for a wide variety of applications. Beyond altering the responsive behavior, the inorganic groups can be harnessed to prepare supramolecular structures and functionalized surfaces/interfaces via covalent crosslinking.[5,33,40,41]

Department of Chemical Engineering and Materials Science, University of Minnesota Twin Cities, 421 Washington Ave SE, Minneapolis, MN 55455, USA. E-mail: mcalab@umn.edu; Tel: +612-625-2551

† Electronic Supplementary Information (ESI) available: [details of any supplementary information available should be included here]. See DOI: 00.0000/00000000.

Polymer thermosensitivity is highly sensitive to physical and chemical alterations in both the polymer and the surrounding environment. In solutions of responsive polymers, small changes in the solvent composition can lead to co-nonsolvency effects, which drastically alter the types of transitions and temperatures at which these transitions occur.[37,38,42,43] Small alterations to the polymer composition can also drastically impact the solution behavior. For example, the upper critical solution temperature of poly(methyl methacrylate) (PMMA) observed in water/ethanol solvent systems can be altered by up to 20 °C with low incorporation (6% mol) of acrylamide comonomers.[43] Additionally, modifying PNIPAM with hydrophobic end groups that are small relative to the polymer molecular weight has been shown to induce micellization below the transition temperature.[44] Recently, Ren and coworkers reported that having different moieties on the α and ω chain ends can alter the assembly and aggregation behavior of PNIPAM, leading to distinct micellization behavior depending on the end group chemistries.[45] The inclusion of an azo end group led to micelles with free chain ends, which caused bridging interactions between the micelles above the thermal transition temperature. This assembly behavior demonstrated a unique signature in calorimetry with two phase separation temperatures.[45] In general, the occurrence of a phase transition in aqueous PNIPAM systems is quite robust, but small modifications can lead to substantial changes in the assembly and aggregation of the thermoresponsive polymers.

The optical transition behavior of aqueous PNIPAM is highly reversible, as the aggregates break up and chains solvate below the LCST. Typically, a hysteresis is observed in the optical response where the cloud point temperature upon heating (T_{CP}) is greater than the clearing temperature upon cooling (T_{Cl}).[46] Though in certain applications, the system may only need to respond to a stimulus one time, repeated reversibility is crucial in applications where the system must respond over many cycles, such as separations,[47] smart windows,[48] or antibiofouling coatings.[49,50] Yet while PNIPAM solutions exhibit thermoreversibility, prior work demonstrates that incorporation of inorganic groups like 3-(trimethoxysilyl)propyl methacrylate (TMA) may lead to irreversible structure changes upon thermal cycling that limit stimuli-responsiveness.[51] Polymer systems containing NIPAM and TMA are of particular interest in coatings,[52] nanoparticles,[2] hydrogels,[6] micelles,[4,23,24] and other applications due to the commercial availability and the structural control enabled by chain growth polymerization of the monomers. Unfortunately, aqueous NIPAM/TMA random copolymers have been shown to demonstrate irrecoverable transmittance upon thermal cycling due to *in situ* silane coupling,[51] where the irrecoverable transmittance is especially pronounced at high TMA incorporation. However in this work, Osváth *et al.*[51] did not investigate the relationship between polymer architecture, assembled structure above the cloud point, and thermoreversibility in solution.

Beyond random copolymers of NIPAM and TMA, polymers containing distinct TMA blocks have been previously synthesized.[53,54] Mellon *et al.*[54] were unable to purify block polymers containing PMMA and TMA due to silane crosslinking.[54] Wu *et al.*[53] synthesized and purified P(NIPAM-b-TMA-b-NIPAM) triblock polymers by using significantly smaller TMA blocks relative to the non-crosslinking monomer than Mellon *et al.*[54] However, the high dispersity of the reported polymers suggests that inter-chain crosslinking likely occurred during purification.[53] An effective strategy to reduce undesired silane coupling is copolymerizing TMA with a different monomer, enabling the synthesis of polymers of controlled architecture and narrow dispersity.[13,23,24] Even in low incorporations, the TMA can be harnessed post-polymerization to prepare supramolecular structures including gels,[25] particles,[2] and surfaces.[52] Note that while the acrylamide analogue of TMA has been polymerized via controlled radical polymerization,[55] this silane-containing acrylamide is of less significant interest for copolymerization with PNIPAM compared to TMA, due to high cost and limited commercial availability, despite potential reactivity advantages.

In this contribution, we explore the connection between polymer composition and architecture to the solution assembly, thermoresponsiveness, and thermal cyclability in aqueous PNIPAM/TMA copolymers containing low TMA mole fractions. Utilizing reversible addition-fragmentation chain transfer polymerization (RAFT), polymers of controlled architecture, molecular weight, and block configuration are synthesized using mild, one-pot reaction conditions to reduce the need for intermediate purification and minimize premature silane hydrolysis and condensation. As no prior study has measured the reactivity ratios when copolymerizing NIPAM and TMA, here the relative monomer reactivities are determined to directly connect polymer architecture with solution structure and optical response. We examine two copolymer architectures: random P(NIPAM-co-TMA), and a 'blocky-functionalized' copolymer where the TMA is localized to one portion of the chain, P(NIPAM-b-NIPAM-co-TMA). Dynamic light scattering (DLS) is used to quantify the role of copolymer architecture and TMA content on the size and dispersity of aggregates formed above the cloud point, whereas cloud point testing (CPT) is used to track the solution opacity and thermoreversibility over multiple thermal cycles. Direct imaging via cryo-transmission electron microscopy (cryo-TEM) is used to confirm formation of distinct structures based on polymer architecture, as identified in DLS. Finally, variable-temperature nuclear magnetic resonance spectroscopy (VT-NMR) is used to connect the chain mobility during and after thermal cycling to the distinct aggregate structures and optical responses identified during DLS and CPT. By uncovering structure-property relationships between polymer architecture and thermal cyclability, we establish design guidelines that could be used to increase the utility and longevity of these inorganic-functionalized responsive polymer systems, potentially enabling scalable advancements in targeted drug delivery, sensing, separations, and energy efficiency.

2 Materials and Methods

2.1 Materials

Acetone (>99.9%), 2-bromoisobutyric acid (98%), deuterium oxide (99.9%), 1,4-dioxane (>99.0%), ethanethiol (97%), ethyl acetate (>99.5%), *n*-hexane (>95%), potassium phosphate tribasic (K_3PO_4, reagent grade), sodium chloride (>99.5%),

sodium trimethylsilylpropanesulfonate (DSS, 97%), and 3-(trimethoxysilyl)propyl methacrylate (98%) were purchased from Sigma-Aldrich and used as received. Dichloromethane (DCM, >99.5%), diethyl ether (99%, stabilized), hexanes (>98.5%), petroleum ether (Certified ACS, boiling range 40-60 °C), sodium sulfate (anhydrous, 99%), tetrahydrofuran (>95%, stabilized) were purchased from Fisher Scientific and used as received. Carbon disulfide (99.9%) was purchased from Acros Organics and used as received. Hydrochloric acid (36.5-38%, ACS grade) was purchased from Macron Fine Chemicals and diluted to 1 M with distilled water. D-chloroform (99.8% + 0.05% vol. tetramethylsilane (TMS)) was purchased from Cambridge Isotope Laboratories, Inc. and used as received. *N*-isopropyl acrylamide (Fisher Scientific, 98%, stabilized) was recrystallized thrice from hexanes and dried *in vacuo* to constant weight. Azobisisobutyronitrile (Sigma-Aldrich, 98%) was recrystallized from methanol thrice and dried *in vacuo* to constant weight.

2.2 Synthesis

2.2.1 Synthesis of 2-(ethylsulfanylthio-carbonylsulfanyl)-2-methylpropionic acid

Chain transfer agent (CTA) 2-(ethylsulfanylthio-carbonylsulfanyl)-2-methylpropionic acid (EMP) was synthesized following Schmidt et al.[56] First, 7.22 g K_3PO_4 (0.0314 mol; 1.1 equiv) was dissolved in 103 mL acetone (1.388 mol; 48.6 equiv) in a 500 mL round bottom flask. Under dynamic nitrogen flow, 2.47 mL ethanethiol (0.0343 mol; 1.2 equiv) was injected and the flask stirred for 20 minutes at room temperature. 5.17 mL carbon disulfide (0.0857 mol; 3 equiv) was then injected and stirred for 20 minutes. Following the addition of carbon disulfide, the solution turned yellow. The vessel was then cooled in an ice bath for 5 minutes, after which 4.77 g 2-bromoisobutyric acid (0.0285 mol; 1 equiv) was added. The reactor was stirred overnight at room temperature under inert conditions. After approximately 18 hours, 348.2 mL 1 M HCl (0.0348 mol acid; 12.19 equiv) was added and the aqueous phase was extracted with 300 mL DCM. The organic phase was then washed once with HPLC grade water (approximately 250 mL) and twice with 10% wt. sodium chloride brine solution (250 mL each). The organic phase was then dried using sodium sulfate for 20 minutes. The sodium sulfate was removed via vacuum filtration and the filtrate was condensed with rotary evaporation, leaving an oily yellow product. This product was purified via column chromatography with silica gel and using an eluant solution of n-hexane:ethyl acetate (2:1 vol:vol). Yellow bands corresponding to EMP were collected and dried with rotary evaporation. The product was recrystallized in n-hexane and dried *in vacuo*, yielding a yellow crystalline product. ^{1}H NMR (500 MHz, $CDCl_3$) δ (ppm) 11.09 (s, 1H), 3.30 (q, J = 7.4 Hz, 2H), 1.73 (s, 6H), 1.34 (t, J = 7.4 Hz, 3H). ^{13}C NMR (126 MHz, $CDCl_3$) δ (ppm) 179.09, 55.62, 31.28, 25.21, 12.88. Spectra shown in SI.1.1.

2.2.2 Copolymer synthesis

All polymers in this contribution were synthesized via reversible addition-fragmentation chain transfer polymerization (RAFT) using EMP as the CTA and azobisisobutyronitrile (AIBN) as the initiator. The following procedure describes a synthesis of P(NIPAM-co-TMA) with M_n = 50 kDa and F_{TMA} = 4% mol. In other syntheses, F_{TMA} was varied by altering the monomer feedstock composition. Stock solutions of EMP and AIBN in 1,4-dioxane were prepared at 25 mg/mL and 1 mg/mL, respectively. 3.26 g NIPAM (28.8 mmol), 0.285 mL TMA (1.2 mmol), 448.7 μL EMP stock solution (0.05 mmol), 821 μL stock solution AIBN (0.005 mmol), and 13.7 mL 1,4-dioxane were added to a 25 mL polymerization flask, yielding $[M]_0$ = 2 M. A stir bar was added and the flask sealed with a septum. The flask was then agitated vigorously to dissolve the NIPAM. Once the reaction mixture was clear, the solution was degassed via three freeze/pump/thaw cycles. A slight positive pressure of nitrogen was maintained to prevent oxygen contamination. A zero-time aliquot was withdrawn to confirm the initial monomer feedstock composition via NMR. The flask was then lowered into a 70 °C oil bath and stirred vigorously. Reaction conversion was monitored by ^{1}H NMR and SEC with regularly drawn aliquots. The reaction was typically quenched between 75-85% conversion, typically around 3.5 h, in liquid nitrogen and opened to air. For purification procedure, see SI.2.

2.2.3 One-pot synthesis: blocky-functionalized copolymers

Blocky-functionalized copolymers were synthesized by initiating a NIPAM homopolymerization and then injecting TMA later in the reaction. Given the small volume of TMA injected, no additional degassing was required. The NIPAM homopolymerization was initiated after degassing and reacted to 30-50% conversion (typically 1.5 h to 2.5 h) prior to injecting the TMA. Aliquots were withdrawn for characterization via SEC and NMR to measure M_n of the PNIPAM homopolymer block and the feedstock ratio after injection, and to estimate NIPAM conversion. A general reaction scheme is shown in Scheme 1.

2.3 Reactivity ratio measurement

Reactivity ratios were estimated using a series of reactions with different monomer feedstocks of NIPAM and TMA. For each reaction, the following stoichiometry was used: $[M]_0:[CTA]_0:[I]_0 = 600:1:0.05$ with $[M]_0 = 3\,M$ in 1,4-dioxane. EMP was used as the CTA and AIBN was used as the initiator. The following monomer compositions were characterized, where f_{TMA} is the mol % of TMA in the initial monomer feedstock: f_{TMA} = 5, 10, 15, 25, 35, 45, 55, 65, 75, 85% mol. The procedure for these measurements is detailed in SI.3.2. Individual monomer conversions were measured via ^{1}H NMR spectroscopy. The aliquot closest to 10% mol total monomer conversion was used to fit the reactivity ratios.

2.4 Tracking monomer conversion via ^{1}H NMR

The conversion of each monomer was tracked via ^{1}H NMR (400 MHz, in $CDCl_3$) during polymerization. The methoxysilyl protons (δ: 3.57 ppm, *s*), shown as A in SI.3.6 were used as an internal standard in both reaction mixture conversion tracking and in analyzing the final product. NIPAM conversion was tracked using the proton trans to the amide in NIPAM (δ: 5.60 ppm, *dd*), shown as D in Fig. SI.3.7. The proton trans to the ester in TMA (δ: 5.53

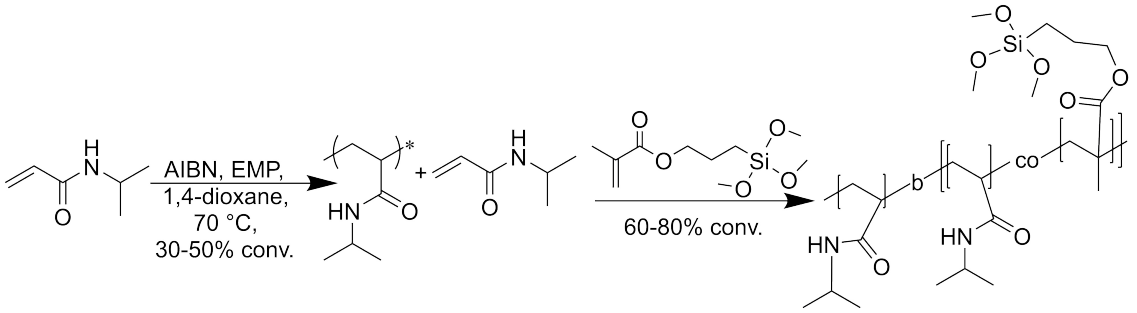

Fig. 1 Synthetic scheme for blocky-functionalized PNIPAM-co-TMA copolymers.

ppm, *t*), labelled B, was used to monitor TMA conversion. The use of these peaks for conversion tracking was confirmed by comparing the individual monomer conversions at the end of a reaction to the composition of the final product, as discussed below. The alkene peak assignments discussed in this section have been confirmed using 2D NMR techniques, discussed in SI.3.8. Tracking monomer conversion from the reaction feedstock enables measuring the monomer incorporation into the copolymer, and thus estimating the reactivity ratios, without needing to purify copolymers with high TMA content.

2.5 SEC-MALS

Size exclusion chromatography with multi-angle light scattering (SEC-MALS) was used to characterize the molecular weight, molar mass distribution (MMD), and dispersity ($Đ$) of the synthesized polymers. Measurements were obtained using an Agilent 1200 series HPLC equiped with a Viscotek column. The refractive index detector is an Optilab T-rEX and the MALS detector is a Wyatt DAWN HELIOS. The mobile phase is dimethyl formamide (DMF) with 50 mM lithium bromide to reduce column interactions in acrylamides. Samples were prepared at 1 mg/mL and filtered through a 0.22 μm polytetrafluoroethylene (PTFE) syringe filter before analysis. To reduce contamination, the first several drops from the syringe filter were discarded. For homopolymer PNIPAM, $\frac{dn}{dc} = 0.0737$ was used to analyze aliquots of unknown concentration. This value for $\frac{dn}{dc}$ was measured using EMP-PNIPAM samples of known concentration using software associated with the refractive index detector assuming 100% mass recovery and a known concentration. For all copolymer samples, the $\frac{dn}{dc}$ values were similarly measured with a sample of known concentration of the purified final product.

2.6 Dynamic light scattering

Dynamic light scattering (DLS) was used to characterize the hydrodynamic diameter (D_h) of the polymers in solution as a function of temperature, which is useful in monitoring the assembly of unimers into aggregates above T_{CP} and to elucidate permanent structure formation as due to *in situ* crosslinking. Samples were prepared at 10 mg/mL in triple distilled water and shaken at 4 °C until dissolved. The samples were then diluted to 1 mg/mL and filtered (0.22 μm PTFE) into PMMA cuvettes. This dilution procedure was used to increase accuracy when preparing the low concentration polymer solutions. Note that room temperature scans of filtered solutions at 1 and 10 mg/mL show similar unimer size (Fig. SI.6.1). A Malvern Zetasizer nanoseries DLS was used in size measurement mode. An automated protocol was implemented which varied the temperature at the following discrete temperatures: 25, 30, 34, 38, and 42 °C. After heating, cooling measurements were taken at 38, 34, 30, and 25 °C. After each measurement, the temperature of the sample was rapidly heated or cooled to the next set point. To reduce thermal inhomogeneities, samples were equilibrated for 3 min at each temperature before data collection. Three measurements of 10 runs of 10 s were obtained at each temperature. Autocorrelation functions and size distributions were fit using the Zetasizer software.

2.7 Cryogenic transmission electron microscopy

Analogous to sample preparation for DLS, samples for cryogenic transmission electron microscopy (cryo-TEM) of N_{456}/T_2 and $N_{283}[N_{113}/T_8]$ were prepared at 10 mg/mL in triple distilled water and shaken at 4 °C until dissolved. The samples were then diluted to 1 mg/mL and filtered (0.22 μm PTFE). N_{456}/T_2 and $N_{283}[N_{113}/T_8]$ were selected for analysis via cryo-TEM because these polymers displayed the greatest difference in size as measured by DLS, and could thus inform the range of sizes and structures observed in the TMA-containing PNIPAM. The solutions were equilibrated at 42 °C for approximately 10 minutes prior to deposition (3 μL) onto perforated carbon support film on a copper TEM grid (lacey Formvar/ carbon films on plasma treated, 200 mesh Cu grids, Ted Pella, Inc., Redding, CA, U.S.A). Sample deposition and blotting were performed in a FEI Vitrobot system (Thermo Fisher Scientific), kept at 42 °C and 100% relative humidity. After blotting, the grids were plunged into liquid ethane at its freezing point for vitrification. The specimens were examined by FEI Tecnai G2 F30 field emission gun TEM, operated at an accelerating voltage of 300 kV, using a Gatan 626 cryo-holder, maintained at –175 °C. Images were digitally recorded using a Gatan UltraScan 4000 4k by 4k CCD camera.

Micrographs were analyzed using ImageJ software to determine the structure sizes and distributions for each sample. The area of each visible structure was determined using the ellipse tool, from which an average diameter (assuming a circular area) is calculated, denoted D_{TEM}. Overlapping structures were distinguished from merging structures by the intensity change in the overlapping region and were sized individually.

2.8 Cloud point testing

To quantify the thermoresponsiveness of each polymer solution, cloud point testing was used to measure light transmittance as a function of temperature; measurements using a violet laser (405 nm, 5 mW) (see SI.8.1) were confirmed with supplementary experiments using a red laser (650 nm, 5 mW). Samples were prepared by dissolving the polymers in triple distilled water at 10 mg/mL. The samples were then shaken at 4 °C until dissolved and then filtered through glass wool into PMMA cuvettes. A series of temperature ramps and equilibration steps were then performed using an automated script to reduce inconsistencies between experiments. Given that the extent of silane hydrolysis depends both on time and temperature, standardizing equilibration times between temperature ramps enables comparisons between samples. First, the temperature of the sample was set to 20 °C and equilibrated for 5 minutes. Then, the sample was heated at a rate of 0.2 °C/min to 45 °C. Prior to cooling, the sample was held at 45 °C for 5 minutes. The sample was then cooled to 20 °C at 0.2 °C/min. This heating/cooling cycle was typically repeated 3 more times to characterize the changes in thermal response due to temperature cycling.

Cloud (T_{CP}) and clearing point (T_{Cl}) temperatures were determined by taking the inflection point in the transmittance measurements (see SI.9). To characterize this inflection point of the transition and the transition widths during heating and cooling in CPT experiments, a Lorentz peak was fit to the smoothed first derivative of transmission with respect to temperature (see Fig. S71). From these fits, four parameters were extracted: T_{CP}, T_{Cl}, heating transition width (w_H), and cooling transition width (w_C). T_{CP} and T_{Cl} were extracted from Lorentz peak maxima, where w_H and w_C were extracted from the full width at half maximum.

2.9 Variable-temperature NMR (VT-NMR)

Samples for VT-NMR experiments were prepared by dissolving the purified polymers into D_2O at 10 mg/mL with 0.01 mg/mL of sodium trimethylsilylpropanesulfonate (DSS) as the reference standard. The solutions were agitated at 4 °C until homogeneous. The solution was filtered through glass wool before adding to the NMR tube. All variable-temperature NMR (VT-NMR) experiments were performed on a Bruker Avance III 500 equipped with a 5 mm BBFO "SmartProbe" with z-axis gradients. 1D ^{1}H NMR spectra were obtained at the following set temperatures: 296, 300, 305, 310, and 314 K. Note that these set points were kept standard between experiments and the sample temperature was extracted as described in the Fig. SI.13. Spectra were obtained in both heating and cooling at the specified temperatures. The temperature of the sensor was allowed to equilibrium, then the probe was tuned (^{1}H = 500.3 MHz), the sample was shimmed, and receiver gain adjusted. At each temperature, 32 scans were obtained with a relaxation delay of 10 s. Approximately 12-13 minutes elapsed between the the scans at each temperature, where the scans took 7 minutes, and the temperature adjustment/equilibration and shimming took the remainder.

After obtaining the spectra, a standardized processing procedure was followed. First, zero filling was used to increase S/N. Then, the spectra were manually phased using the solvent peak. A multipoint baseline correction was applied, where baseline points were selected at similar chemical shifts to reduce bias. The DSS peak was referenced to 0 ppm and the integration of the solvent peak was normalized to 1. Note that this HOD peak shifts upfield with increasing temperature, though the integration remains consistent over the temperature range analyzed. An immobilization factor, p, was defined by:

$$p = 1 - \frac{I_T}{I_{ref}} \quad (1)$$

where I_T is the integral intensity of a signal at temperature T and I_{ref} is the integral intensity at a reference temperature, where all integral intensities are relative to the solvent peak. In these studies, this reference temperature was the first scan at the low temperature prior to thermal cycling.

3 Results and discussion

3.1 Polymer synthesis

3.1.1 Determining monomer reactivity ratios in RAFT

To quantify the relative reactivity and comonomer incorporation into the copolymer, reactivity ratios were determined via three fitting methods: Fineman-Ross,[57] Kelen-Tüdős,[58] and least-squares fit.[59] Calculated reactivity ratios for each method demonstrate that TMA is preferentially incorporated at all monomer feedstock compositions (Table 1); measured instantaneous TMA incorporation and associated fits are shown in Fig. 2. Deviations from the fits are likely due to slight differences in the overall reaction conversion used to determine instantaneous monomer incorporation.

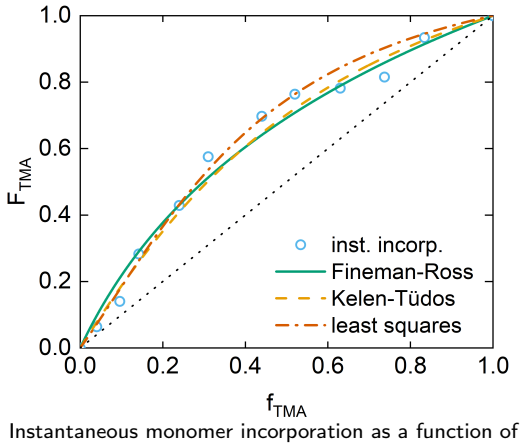

Fig. 2 Instantaneous monomer incorporation as a function of monomer feedstock (blue ○). While reactivity ratios from different fitting methods vary (Table 1), all methods indicate preferential TMA incorporation for all monomer feedstocks. Dotted black line is given as a reference to ideal copolymerization, where the two reactivity ratios are equal.

Table 1 Reactivity ratios fit using common methods.

Fitting method	r_{TMA}	r_{NIPAM}
Fineman-Ross	2.1	0.38
Kelen-Tüdős	2.6	0.51
least squares	3.7	0.58

Monomer conversions were monitored with ^{1}H NMR to track the change in integral intensity of the monomer alkene peaks in time, eliminating the need to purify polymer products of high

TMA content. As TMA incorporates into the copolymer at a higher rate than NIPAM, the feedstock composition drifts with reaction conversion. As a result, copolymers likely have a slight gradient in composition, where one end of the chain has a higher density of TMA than the other; though, due to the low TMA content in the monomer feedstock, the effect is likely minimal. The copolymerization of NIPAM and TMA is moderately ideal, as $r_{TMA} \cdot r_{NIPAM} \approx 1$, but $r_{TMA} > 1$ and $r_{NIPAM} < 1$.[60] This moderately ideal copolymerization suggests that the monomers have similar relative reactivity, with a propensity to incorporate higher quantities of TMA in the copolymer.

Given the lower general rate of polymerization of methacrylates in comparison to acrylamides, the expected result would be preferential incorporation of the NIPAM (see SI.3.1 for more detail).[51,60] The discrepancy between prediction and observation can be attributed to the differences in monomer chemical structure and the RAFT polymerization conditions. Compared to free radical polymerization, the inclusion of a chain transfer agent has been reported to alter the reactivity of the comonomers;[59,61] further studies are necessary to decouple potential contributions from both CTA and solvent. For systems in this study, this surprising result is advantageous, as TMA incorporation in the polymers is low. If the reactivity ratios were reversed, synthesizing these copolymers would be difficult due to the preferred incorporation of NIPAM in addition to the predominantly NIPAM feedstocks.

3.1.2 Polymer characterization via ^{1}H NMR

Thermosensitive behavior, cyclability, and structure-formation were explored extensively for random copolymers and blocky-functionalized copolymers at low TMA contents only ($\leq$3.5% mol), given previous reports of irreversible structure formation and loss of thermosensitivity at high TMA contents due to silane coupling.[51] Note that higher TMA content polymers are difficult to synthesize and purify while maintaining products of controlled Đ; see SI.5.1 for data on higher TMA contents. Copolymers and blocky-functionalized copolymers were synthesized via a one-pot procedure to increase scalability and to reduce intermediate purification, which could cause undesired silane hydrolysis. A product summary is given in Table 2; all copolymers had similar M_n (47-55 kDa). To calculate the molar content of TMA in the purified polymer, F_{TMA}, the following equation is used:

$$F_{TMA} = 1 - \frac{I_{4\ ppm} - 2}{I_{4\ ppm} - 1} \quad (2)$$

where $I_{4\ ppm}$ is the integration of the peak corresponding to the methine proton of the NIPAM isopropyl group and the methylene protons adjacent to the ester in TMA (δ: 4.0 ppm, *b*), as shown in Fig. 3E and C, respectively. Note that equation 2 assumes that the integration of the methoxysilane protons (δ: 3.57 ppm, *s*) is normalized to 9. Subtracted terms result from peak overlap between the methine proton in the isopropyl group of NIPAM and the methylene protons adjacent to the ester in the TMA. Two peaks are labeled **D** in Fig. 3 due to the presence of free and hydrogen-bonded amide protons in d-chloroform.[62]

Osváth and coworkers[51] report that several prior works fail to account for this overlap, resulting in an overestimate of F_{NIPAM},[13,63] but provide no additional evidence. To confirm overlapping signals, the ^{1}H-^{13}C heteronuclear single quantum coherence spectroscopy (HSQC) was performed. In a spectrum of the final copolymer product (SI.3.9), two distinct resonances of opposite polarities can be seen in the ^{13}C spectrum at 4 ppm in the ^{1}H spectrum, confirming the overlapping signals in ^{1}H NMR spectra. Close agreement was found between the F_{TMA} calculated using Equation 2 and the individual monomer conversions from aliquots taken immediately prior to quenching the reaction. Reaction stoichiometries and individual monomer conversions for each sample can are listed in Table S1.

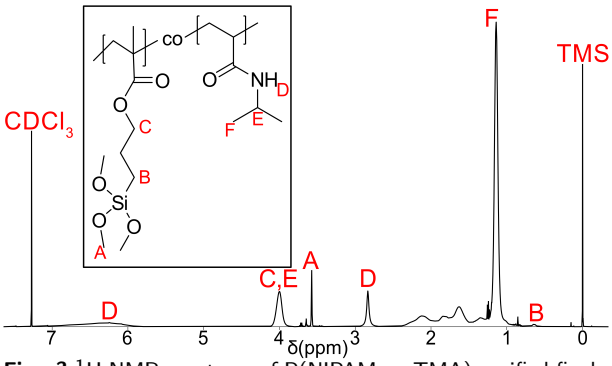

Fig. 3 ^{1}H NMR spectrum of P(NIPAM-co-TMA) purified final product.

3.1.3 Polymer characterization via SEC-MALS

Size exclusion chromatography confirmed the successful formation of blocky-functionalized polymers and showed the purification procedure had minimal impact on the molecular weight due to silane coupling (Fig. 4). Given the propensity for silane hydrolysis and condensation upon exposure to moisture, minimizing silane coupling during the purification procedure is essential to maintain a low dispersity product. Copolymers are all of similar molecular weight with low dispersity ($Đ < 1.2$, Table 2).

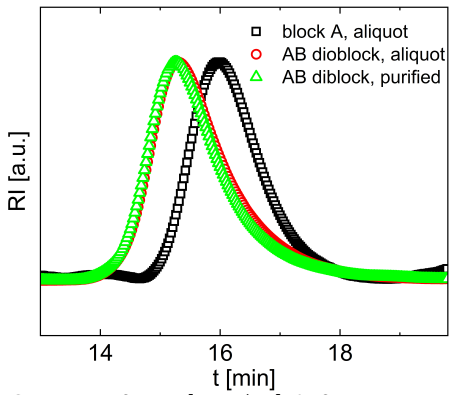

Fig. 4 SEC traces of $N_{293}[N_{143}/T_8]$ before injecting TMA, before quenching, and after purifying shows successful growth of TMA-functionalized B-block; crosslinking during purification is avoided.

Three refractive index traces for the blocky-functionalized copolymer P(NIPAM$_{293}$-b-NIPAM$_{143}$-co-TMA$_8$) exhibit a clear shift to lower retention times from the A block to the AB diblock, confirming successful chain extension (Fig. 4). This polymer is denoted $N_{293}[N_{143}/T_8]$, and consists of a final product with M_n = 50.1 kDa, $Đ$ = 1.10, and overall TMA fraction $F_{TMA,AB}$ = 1.9% mol. As seen in Fig. 4, the trace from an aliquot taken im-

Table 2 Table listing synthetic products of controlled dispersity. See Table S1 for reaction stoichiometries and monomer conversions.

Polymer	Abbreviation	M_n[a] (kDa)	$Đ$[a]	$F_{TMA,AB}$[b] (% mol)	$F_{TMA,B}$[a,b] (% mol)	$T_{CP,1}$[c] (°C)	$T_{Cl,1}$[c] (°C)
P(NIPAM$_{408}$)	N_{408}	46.2	1.13	0	–	34.0	31.2
P(NIPAM$_{479}$)	N_{479}	54.2	1.15	0	–	33.1	30.9
P(NIPAM$_{540}$)	N_{540}	60.7	1.09	0	–	34.6	31.9
P(NIPAM$_{456}$-co-TMA$_2$)	N_{456}/T_2	52.1	1.11	0.5	–	33.1	30.7
P(NIPAM$_{400}$-co-TMA$_{14}$)	N_{400}/T_{14}	48.7	1.19	3.5	–	33.1	–
P(NIPAM$_{337}$-b-NIPAM$_{88}$-co-TMA$_3$)	$N_{337}[N_{88}/T_3]$	48.7	1.10	0.6	3.2	33.2	30.6
P(NIPAM$_{363}$-b-NIPAM$_{113}$-co-TMA$_5$)	$N_{363}[N_{113}/T_5]$	55.0	1.07	1.0	4.2	32.8	30.0
P(NIPAM$_{293}$-b-NIPAM$_{143}$-co-TMA$_8$)	$N_{293}[N_{143}/T_8]$	50.3	1.10	1.9	5.2	32.8	27.3
P(NIPAM$_{283}$-b-NIPAM$_{113}$-co-TMA$_8$)	$N_{283}[N_{113}/T_8]$	46.8	1.10	2.0	6.6	33.5	31.0

[a]Determined via SEC-MALS (SI.5). [b] Determined via ^{1}H NMR spectroscopy (SI.4). [c]Determined via cloud point testing (λ = 405 nm, SI.11).

mediately before TMA injection (black □) corresponds to the homopolymer PNIPAM A-block; corresponding traces after growth of the P(NIPAM-co-TMA) B-block before (red ○) and after purification (green △) appear at earlier retention times.

The traces of the unpurified and purified final product overlap closely with no major shifts or appearances of new peaks or shoulders. The final product shows a slight decrease in intensity at lower molecular weights (higher retention times), likely due to the purification procedure in which higher molecular weight polymer chains preferentially precipitate.[64] The close overlap suggests that silane crosslinking during the workup procedure is minimal and does not substantially impact the MMD. SEC traces of the remaining polymers can be seen in SI.5.

3.2 Structural transitions relative to thermal transitions

Dynamic light scattering confirmed that blocky-functionalized copolymers of P(NIPAM-co-TMA) exhibited structural transitions corresponding to the temperature of PNIPAM phase separation, resulting in the formation of aggregates of low hydrodynamic diameter (D_h) with low polydispersity (*PDI*). Note that *PDI* corresponds to the polydispersity of the structure measured in DLS, and not the dispersity ($Đ$) of the molar mass distribution as measured by SEC-MALS. Representative intensity probability distributions during heating and cooling are shown in Fig. 5 for a blocky-functionalized copolymer with average structure P(NIPAM$_{283}$-b-NIPAM$_{113}$-co-TMA$_8$), referred to as $N_{283}[N_{113}/T_8]$ (M_n = 47 kDa, $Đ$ = 1.1); for raw data from other blocky-functionalized copolymers, see SI.6. While this polymer has approximately 2% mol TMA, these repeat units are concentrated across ~30% wt. of the chain. At room temperature both prior to heating and following cooling, $N_{283}[N_{113}/T_8]$ exhibits a bimodal size distribution (Fig. 5). The low D_h peak corresponds to solvated unimers, whereas the high D_h peak that forms reproducibly suggests that some aggregation occurs at ambient conditions.

Upon heating to 30 °C, the intensity of the unimer peak decreases, while that of the larger aggregate peak increases and shifts to smaller length scales (Fig. 5a), suggesting that unimers begin forming denser aggregates as the chains collapse. Upon further temperature elevation, the unimer peak disappears entirely, leaving only a narrow peak corresponding to the secondary structure. At the highest temperature (42 °C), the single peak at D_h = 120.7 ± 0.8 nm with narrow polydispersity (*PDI* = 0.035) suggests controlled self-assembly, as similar systems without localized TMA groups display a larger and broader aggregate peak (Fig. 6a; see SI.6). For example, copolymer PNIPAM$_{456}$-co-TMA$_2$

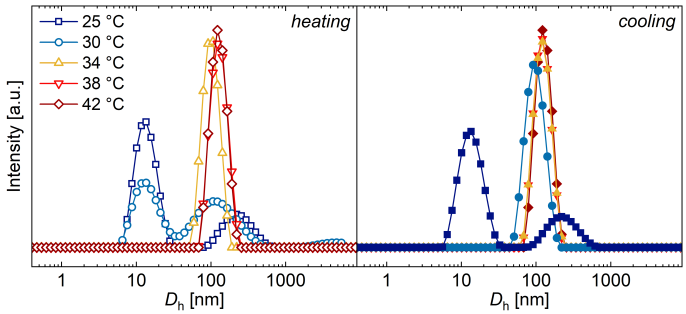

Fig. 5 Intensity probability distribution of P(NIPAM$_{283}$-b-NIPAM$_{113}$-co-TMA$_8$) upon heating and cooling. Upon heating, the bimodal distribution shifts into a single intense peak. Upon cooling, the two size populations re-emerge.

(N_{456}/T_2, M_n = 52.1 kDa, $Đ$ = 1.11) under similar conditions has a hydrodynamic diameter and *PDI* that are both three-fold larger (D_h = 371 ± 4 nm, *PDI* = 0.12). In this latter system, TMA only minimally impacts structure formation compared to homopolymer controls (Fig. S56), given the average of two repeat units per chain. As the two polymers have similar M_n and $Đ$, the increased functionalization and localization of the TMA repeat units in the blocky-functionalized copolymer leads to distinct aggregation behavior at elevated temperatures.

Additional DLS measurements on polymers with similar molecular weights but different TMA functionality and architecture confirm that increased TMA functionalization and localization leads to formation of smaller structures with narrow *PDI* above the cloud point, T_{CP} (Fig. 6, Table 2). However, all polymers transition from unimers to larger-scale structures upon heating (intensity distributions in D_h at 42 °C for all samples shown in Fig. S55). These temperature-dependent hydrodynamic diameters are summarized in Fig. 6a for homopolymers and random copolymers, and in Fig. 6b for blocky-functionalized copolymers. For raw DLS data, see SI.6; for DLS on additional homopolymers given in Table 2, see Fig. S57. In Fig. 6, a hysteresis is observed where the transition back to unimers occurs at a lower temperature during cooling (closed symbols) than upon heating (open symbols), which is attributed to the additional kinetic processes involved in aggregate breakup and chain solvation.[46,65]

The copolymer with the lowest TMA content, N_{456}/T_2, forms the largest structures at elevated temperatures (D_h = 371 ± 4 nm, Fig. 6a), as the responsive behavior is dominated by the PNIPAM character. A small decrease in aggregate size is seen in $N_{337}[N_{88}/T_3]$ (D_h = 324 ± 2.6 nm, Fig. 6b), where a simi-

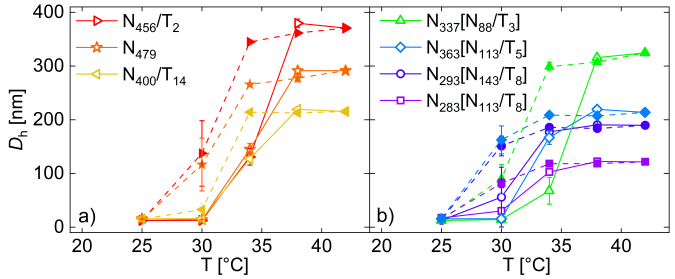

Fig. 6 Structural transitions in PNIPAM-containing polymers (open symbols: heating, closed symbols: cooling). a) Homopolymers and random copolymers form large aggregates with *PDI* ≈0.1 above 40 °C. Differences in D_h and *PDI* are largely driven by M_n. b) For similar M_n, blocky-functionalized copolymers have small D_h and low *PDI*s at $T > 40$ °C, with both properties controlled primarily by TMA content. At high T, error bars are smaller than symbols. See Fig. S56 for *PDI* vs. T.

lar TMA content is instead localized. The structures formed from polymers with low TMA incorporation above T_{CP} are polydisperse (*PDI* >0.1) and demonstrate D_h larger than corresponding homopolymer controls. This phenomenon could arise due to light crosslinking effectively increasing the chain molecular weight, while minimally affecting the hydrophobicity of the chain. Higher incorporation of hydrophobic TMA causes a greater degree of chain collapse, as seen in copolymer N_{400}/T_{14} (D_h = 215.4 ± 2.5 nm, *PDI* = 0.088, Fig. 6a).

Blocky localization of TMA has a dramatic impact on aggregate size at elevated temperatures, where blocky-functionalized $N_{283}[N_{113}/T_8]$ forms the smallest structures above T_{CP} (Fig. 6b). This polymer has nearly half the TMA units of $[N_{400}/T_{14}]$, but an average hydrodynamic diameter and *PDI* that are nearly two-fold and 2.5-fold smaller, respectively. Further, the blocky functionalized $N_{363}[N_{113}/T_5]$ has a statistically identical size and *PDI* to $[N_{400}/T_{14}]$ at 42 °C, despite having one-third the TMA content and a larger M_n. These two comparisons suggest that: (1) D_h and *PDI* depend strongly on both TMA content and TMA localization, and (2) beyond increased chain collapse, TMA localization promotes assembly of controlled structures, such as micelles, above T_{CP}. Micelle formation was recently reported in TMA-containing PNIPAM by Wu and coworkers.[53] These systems had discrete TMA B-blocks, as opposed to blocky functionalization, leading to core/shell micelles that formed at room temperature. Further, the ABA triblock-containing micelles used by Wu et al. formed large, polydisperse structures above T_{CP}, and had higher TMA contents than any blocky-functionalized copolymer here.

In other blocky-functionalized systems, small structure sizes most strongly correlate with higher TMA content in the B-block, $F_{TMA,B}$ (Fig. 6b, Table 2); see Fig. S58a for multivariate analysis. Here, the hydrodynamic diameters above T_{CP} are not as well-described by the number of TMA units in the B-block or total TMA content, $F_{TMA,AB}$. For example, $N_{283}[N_{113}/T_8]$ and $N_{293}[N_{143}/T_8]$ both contain 8 TMA units in the B-block. However, despite similar *PDI*, D_h is nearly 60% larger in $N_{293}[N_{143}/T_8]$, which has $F_{TMA,B}$= 5.2% mol vs. 6.6% mol in $N_{283}[N_{113}/T_8]$ (Table 2). While $N_{293}[N_{143}/T_8]$ has a 7.5% larger M_n than $N_{283}[N_{113}/T_8]$, its D_h is much closer in size to $N_{363}[N_{113}/T_5]$, which is ∼10% larger in M_n but has a more similar $F_{TMA,B}$ (4.2% mol). Unsurprisingly, D_h and *PDI* for blocky-functionalized copolymers are also strongly correlated (Fig. S58b); however, no further reductions in *PDI* are observed for B-block TMA contents above ∼5%.

To deconvolute these potential molecular weight effects, a series of PNIPAM homopolymers ($Đ < 1.2$, M_n =46-61 kDa) were compared via DLS (Fig. S57). While both D_h and *PDI* at 42 °C increase with molecular weight, the observed parameter ranges are substantially narrower than those observed in TMA-containing polymers. For example, above T_{CP}, D_h for homopolymer controls ranges from 277 to 324 nm with corresponding *PDI* from 0.12 to 0.17 (Fig. S57). As all TMA-containing polymers fall within the M_n range of the controls, the observed differences in D_h and *PDI* cannot be attributed to molecular weight. Multivariate analysis of parameters associated with the blocky-functionalized copolymers confirms this conclusion, where no correlation is observed between M_n and D_h or M_n and *PDI* (Fig. S58c).

In summary, the size of the aggregated structure above the LCST decreases both with increasing TMA content and with TMA localization, where fewer localized TMA units ($N_{283}[N_{113}/T_8]$) can more effectively reduce the cluster size than a large number of TMA units distributed randomly along the chain (N_{400}/T_{14}). The aggregate size and dispersity are affected by both TMA content and localization, where constraining the TMA units to one region of the chain can lead to the formation of structures nearly one-third the size of those formed in homopolymer controls of comparable molecular weight. As TMA increases the hydrophobicity of the PNIPAM chain, one possible explanation is that the blocky localization drives formation of micelle-like structures despite the limited number of TMA blocks per chain, where the core is composed of the more hydrophobic TMA-containing block. These DLS experiments highlight the surprising impact of low TMA incorporation (<4% mol total) on the aggregate structures formed in PNIPAM above T_{CP}, which is promising for applications requiring a high degree of responsivity and cyclability that may be negatively impacted by the continued coupling of silane groups.

3.3 Confirming aggregate structure via cryo-TEM

Direct imaging of the aggregates formed by copolymer N_{456}/T_2 and blocky-functionalized copolymer $N_{283}[N_{113}/T_8]$ above T_{CP} supports DLS results, further suggesting that $N_{283}[N_{113}/T_8]$ forms smaller and more controlled aggregate structures than N_{456}/T_2. Despite differences in the TMA content and chain configuration, these polymers were selected because one formed the smallest and the other the largest structures in DLS measurements. Therefore, direct imaging could inform the range and type of structures formed at elevated temperatures. Cryo-TEM micrographs of both polymers show the formation of dominantly spherical and merging aggregate structures (Fig. 7a-b,e-f; see Figs. S66, S67, and S68 for additional micrographs); however, N_{456}/T_2 displays a wider range of structure sizes. In particular, N_{456}/T_2 contains several very large structures (D_{TEM} > 80 nm, Fig. 7d) absent from blocky-functionalized $N_{283}[N_{113}/T_8]$; these observations are consistent with visual inspection of the equilibrated polymer solutions prior to deposition on the grids, where $N_{283}[N_{113}/T_8]$ is less opaque and has a stronger blue tint

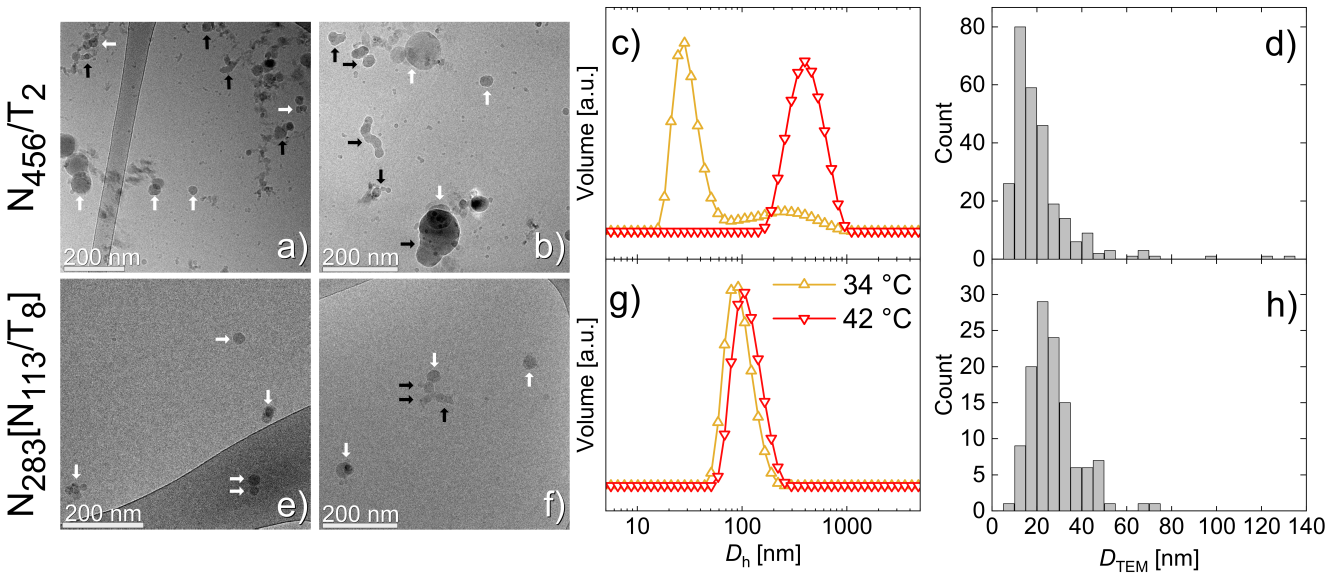

Fig. 7 Comparison of cryo-TEM and DLS results for copolymer N_{456}/T_2 (a-d) and blocky-functionalized $N_{283}[N_{113}/T_8]$ (e-h). Solutions were deposited above T_{CP} and subsequently vitrified prior to imaging. (a-b) Cryo-TEM micrographs of N_{456}/T_2. (e-f) Cryo-TEM micrographs of $N_{283}[N_{113}/T_8]$. Black arrows denote merging structures, white arrows denote individual or overlapping structures. (c,g) The shapes of the DLS volume-averaged size distributions at 34 °C compare favorably with aggregates sized from cryo-TEM micrographs (d,f). Note that the DLS volume distribution is used to enable more accurate comparison to imaging, as intensity distributions are heavily influenced by large structures.

than N_{456}/T_2, indicating smaller light scattering structures (Fig. S62). Additionally, the N_{456}/T_2 micrographs contain a substantial population of small structures ($D_{TEM} \leq 10$ nm) observed only sparingly in $N_{283}[N_{113}/T_8]$, which are likely small clusters of collapsed unimers (Fig. 7d vs. h). The numerous small structures present in N_{456}/T_2 likely exist due to the delayed onset of the thermal transition in N_{456}/T_2 vs. $N_{283}[N_{113}/T_8]$. As seen in the DLS volume distribution at 34 °C (Fig. 7c), N_{456}/T_2 contains at least two populations, with peaks near 30 nm and 280 nm likely corresponding to collapsing unimers vs. aggregates growing through fusion, respectively. Conversely, $N_{283}[N_{113}/T_8]$ has formed a uniform, large population at 34 °C (Fig. 7g), suggesting a more complete transition. As both polymers show a single population at 42 °C, the broad distribution and dispersity in structure sizes in the cryo-TEM likely reflects that N_{456}/T_2 has not formed a stable structure size at lower temperatures. Therefore, the micrograph structures correspond more closely to the DLS data obtained at 34 °C, an earlier point in the thermal transition.

Interestingly, fusion events, where smaller spherical structures coalesce into larger features, are clearly visible in both polymers (indicated with black arrows in Fig. 7a-b, e-f). In Fig. 7b, these events often appear as two spheres neatly merging or as several spheres merging into longer structures with less curvature. This behavior is distinct from overlapped structures, which is easily detected by changes in intensity in overlap regions (overlapping and individual structures indicated with white arrows in Fig. 7). Despite the fact that N_{456}/T_2 requires higher temperatures to fully transition (Fig. 7c vs. g), several large-scale fusion events are observed (Figs. 7b, S67), whereas fusion events are not observed above a critical subunit size of $D_{TEM} \approx 30$ nm in $N_{283}[N_{113}/T_8]$ (Fig. S69). While these large-scale fusion events are rare in the micrographs and additional data is necessary to form definitive conclusions, this observation is consistent with the much larger D_h from DLS in N_{456}/T_2 at elevated temperatures (Fig. 7c,g).

For both polymers, the cryo-TEM structures are smaller than those from DLS (Fig. 7d&h; see S66 for all sized images), due to the differences between the measurements. First, the hydration shell around the structures increases D_h relative to the true structure size. Additionally, D_h is a Z-average measurement, so larger structures have a larger impact on the measurement than small structures. Nevertheless, average diameters are extracted for $N_{283}[N_{113}/T_8]$ and N_{456}/T_2, yielding $D_{TEM} = 27.4 \pm 11$ nm and 21.3 ± 15 nm, respectively. In contrast to DLS findings, the average diameter of N_{456}/T_2 is less than $N_{283}[N_{113}/T_8]$, which can be explained by to the numerous small features in N_{456}/T_2 that do not appear in micrographs of $N_{283}[N_{113}/T_8]$. Thus to more accurately compare the thermally-transitioned structures, the largest 10% of structures were examined, yielding average diameters of $D_{TEM} = 51.5 \pm 8.6$ nm and 56.1 ± 24 nm for $N_{283}[N_{113}/T_8]$ and N_{456}/T_2, respectively. Here, N_{456}/T_2 has both a larger diameter and standard deviation, reflecting the larger D_h and *PDI* observed in DLS at 34 °C and 42 °C. While cryo-TEM and DLS can only be compared semi-quantitatively, direct imaging confirms formation of largely spherical structures, with increased size and dispersity for the largest structures in the copolymer vs. blocky functionalized polymer.

3.4 Impact of low TMA incorporation on solution opacity

To understand the stimuli-responsiveness and cyclability in low TMA-containing copolymers, cloud point testing (CPT) was performed over heating and cooling cycles. CPT is a direct measurement of the changes in light transmittance of the polymer solution as a function of temperature, thus serving as a assessment of the performance and longevity of the polymer systems in optical applications. Optical responses depend on TMA content, with blocky localization leading to distinct behavior on re-

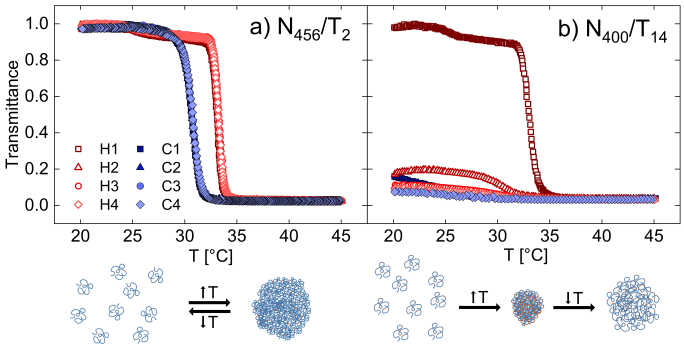

Fig. 8 TMA content impacts the transmittance response of copolymer solutions (10 mg/mL) with thermal cycling: a) N_{456}/T_2; b) N_{400}/T_{14}. Higher F_{TMA} leads to irrecoverable opacity where low F_{TMA} does not significantly alter the thermal response relative to homopolymer controls.

peated cycles. Interestingly, blue hues are observed visually in cycled TMA-containing samples (Fig. S79) and confirmed with UV-vis spectroscopy (Fig. S70). These hues are likely due to the formation of smaller structures with TMA incorporation that scatter light via the Tyndall effect with a λ^{-4} dependence, consistent with DLS results (Fig. 6). Thus a violet laser ($\lambda = 405$ nm) was used increased the signal of the transmittance responses of blocky functionalized samples, though select trials were also verified using a red laser ($\lambda = 650$ nm, SI.12).

Over four cycles, the transmittance changes and recovery for N_{456}/T_2 (Fig. 8a) are similar in appearance to that of homopolymer PNIPAM controls (SI.10), with sharp changes in transmittance upon heating and a slight hysteresis upon cooling that produce distinct cloud point (T_{CP}) and clearing point (T_{Cl}) temperatures. The similarity between N_{456}/T_2 and homopolymer controls in addition to the high transmittance recovery suggest that limited structural changes occur during cycling, likely due to the low density of TMA units that prevent significant crosslinking; this proposed behavior is illustrated in Fig. 8a. Any light inter-chain crosslinking would instead result in chains with a higher effective molecular weight, without restricting conformational transitions. At higher TMA densities, like in N_{400}/T_{14} (Fig. 8b), multiple inter- and intra-chain crosslinks can form at elevated temperatures when chains are collapsed and aggregated, locking the chains into a structure with reduced mobility and solubility even when the temperature is lowered below T_{Cl}. Here, a large drop in transmittance occurs during the first heating cycle (H1), but the transmittance never recovers above 20% upon cooling and the sample retains an opaque white/blue hue (Fig. S78).

Distinct transmittance behavior upon cycling is observed in blocky-functionalized copolymers based on B-block TMA content. As in N_{456}/T_2, low TMA-content $N_{337}[N_{88}/T_3]$ also exhibits a transmittance response upon cycling similar to homopolymer controls (Fig. 9a), suggesting repeated large-scale structure formation with heating and aggregate breakup upon cooling. While the optical response appears qualitatively similar to the homopolymers (SI.10), a slight decrease in transmittance recovery and increase in T_{Cl} are observed over the thermal cycles. The full decrease in transmittance is unsurprising, given that this polymer forms large, disperse aggregates with increasing temperature, as observed via DLS. The reduced number and density of TMA groups also suggests that any silane coupling would result in minimally constrained chains and minimal permanent transmittance loss, similar to N_{456}/T_2. However, light silane coupling likely occurs during cycling for both polymers, resulting in formation of larger aggregates which cause a more pronounced transmittance loss with further cycling; this hypothesis is supported by measurements at $\lambda = 650$ nm, which exhibit a continued decrease in transmittance below T_{CP} with increasing cycle number (Fig. S77). Thus low TMA content does not substantially alter the transmittance response for random or blocky-functionalized copolymers, yielding similar behavior to homopolymers.

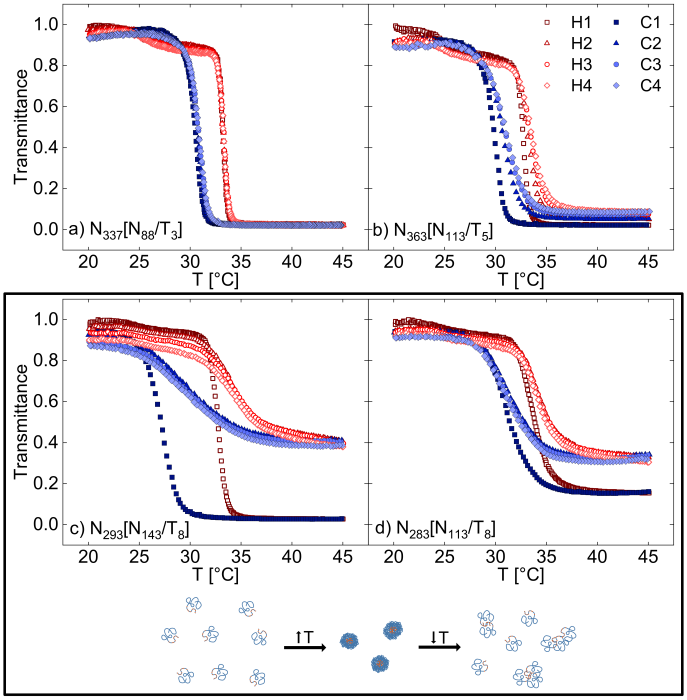

Fig. 9 Blocky-functionalized polymers at 10 mg/mL polymer show different behavior depending on TMA content in B-block at $\lambda = 405$ nm: a) $N_{337}[N_{88}/T_3]$; b) $N_{363}[N_{113}/T_5]$; c) $N_{293}[N_{143}/T_8]$; d) $N_{283}[N_{113}/T_8]$. A higher TMA content leads to a smaller size distribution above T_{CP}, suggesting that the limited thermal response with increasing cycle number in (b) is due to formation of small, well-ordered structures (Fig. 6).

Increasing the TMA content in blocky-functionalized copolymers leads to non-overlapping responses between cycles, shown in Fig. 9b for $N_{363}[N_{113}/T_5]$. This moderately-functionalized polymer never regains complete transmittance at low temperatures nor full opacity at 45 °C with each cycle; thus the transmittance response narrows in both directions. Additionally, the transitions upon both heating and cooling broaden and shift to higher temperatures with cycling. The difference in cycles is greatest between the first and second; the second through fourth cycles overlap more closely. A distinct transmittance response is observed in $N_{293}[N_{143}/T_8]$, where the difference between the first and subsequent cycles is pronounced (Fig. 9c). In cycle one, a complete loss of transmittance occurs with a nearly full recovery. Subsequent cycles show a substantially reduced response, where the transmission does not drop below 40%. A similar response is observed in $N_{283}[N_{113}/T_8]$ (Fig. 9d); the illustration in Fig. 9

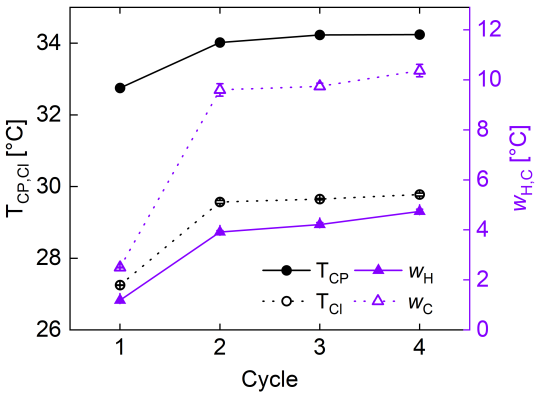

Fig. 10 Critical temperatures (left, ○ ●) and transition widths (right, △ ▲) from CPT for $N_{293}[N_{143}/T_8]$ across four thermal cycles. Substantial increases in transition temperatures and widths are observed after cycle 1, and subsequently plateau on repeated cycling due to the structural formation and subsequent silane coupling at elevated temperatures.

depicts the proposed response for both high TMA content blocky-functionalized copolymers. However, $N_{283}[N_{113}/T_8]$ never has a full transmission loss at high temperatures likely due to its small structure size, retaining ~16% transmittance at 45 °C during the first cycle.

The optical responses of blocky-functionalized copolymers can be rationalized by DLS findings, where smaller structures generally decrease the measured opacity at high temperatures. Similarities between $N_{337}[N_{88}/T_3]$, N_{456}/T_2, and homopolymer controls are attributed to large structure size and *PDI*. Intermediate-sized, fairly polydisperse structures in $N_{363}[N_{113}/T_5]$ scatter light effectively across thermal cycles, though the slight increase in transmittance at 45 °C suggests minor irreversible structure formation in cycle one. For blocky-functionalized copolymers with higher TMA content, the structure size and *PDI* above T_{CP} decrease, substantially altering cyclability. For example, while structures in $N_{293}[N_{143}/T_8]$ are similar in size to $N_{363}[N_{113}/T_5]$, the former structures have substantially lower *PDI*s. In these smaller and more uniform structures, silane coupling upon cycling could permanently fix structures that scatter less light and limit the ability of PNIPAM to reconfigure as it expels water, reducing the optical response. While these smaller structures still produce a transmittance response, the low solution concentration likely prevents aggregation over long length scales during cycling, consistent with decreased responses at 650 nm (Fig. S76b). As $N_{283}[N_{113}/T_8]$ forms the smallest assemblies by far (Fig. 6), a full transmittance loss is not observed and a reduced optical response is seen with cycling. However, the difference between cycles is less pronounced in $N_{283}[N_{113}/T_8]$ than in $N_{293}[N_{143}/T_8]$ (Fig. 9c vs. d), likely due to its initial compact structure size.

Unlike in homopolymers, the thermal transition widths broaden and critical temperatures change with increasing cycle number for blocky-functionalized copolymers. The transition width, w, quantifies the sharpness of the thermal transition upon both heating (w_H) and cooling (w_C). The transition widths are particularly sensitive to localized TMA content, as dramatic increases in both w_H and w_C are observed for blocky-functionalized polymers. The largest increase in w occurs after the first cycle, where the transition broadening is attributed to inter- and intra-molecular crosslinking. Coupling causes chains to be immobilized in a partially collapsed conformation with reduced mobility, thus causing the transition to broaden in both directions. In $N_{283}[N_{113}/T_8]$ and $N_{293}[N_{143}/T_8]$, w_C increases by approximately 2 and 8 °C, respectively (Fig. 10, SI.11). While $N_{283}[N_{113}/T_8]$ has a higher B-block TMA fraction, its shorter B-block length likely contributes to the lower change in w_C upon repeated cycling because a smaller fraction of the total chain can be immobilized via TMA crosslinking. In $N_{293}[N_{143}/T_8]$ (Fig. 10, right axis), a drastic jump in w occurs after the first cycle, after which the transition widths plateau with repeated cycles. Although the change in transmittance with cycling is small for $N_{337}[N_{88}/T_3]$ and $N_{363}[N_{113}/T_5]$, the transition widths with cycling increase similarly to polymers with higher TMA content (Fig. S74). In homopolymer controls, w_C is larger than w_H by ~2-fold across cycles and is relatively consistent across thermal cycles; see SI.11 for more details.

As TMA increases the hydrophobicity of the PNIPAM chain,[51,66] T_{CP} was expected to decrease with TMA incorporation; however here, this behavior is not uniformly observed, likely due to the low TMA incorporation. Wu and coworkers reported a non-monotonic trend between TMA content and the T_{CP} in ABA triblock micelles,[53] attributed to competition between the hydrophobic methoxysilanes and the hydroxysilanes produced during hydrolysis. At high TMA content, the hydroxysilanes were sufficiently hydrophilic to lower T_{CP}. Given the unique assembly properties of the blocky-functionalized copolymers induced by few TMA units, the lack of a clear trend between TMA content and T_{CP} is not surprising, as factors beyond TMA content likely dominate the transition behavior. In the blocky-functionalized polymer samples, the T_{CP} and T_{Cl} increase after the first cycle, and typically plateau upon repeated cycles (Fig. S74). With the exception of $N_{293}[N_{143}/T_8]$, the changes in T_{CP} and T_{Cl} are small, typically < 1 °C (see Fig. 10, left axis for $N_{293}[N_{143}/T_8]$; SI.11 for other samples). These small changes are likely due to the large PNIPAM blocks dominating the responsive behavior. The observed increase in T_{CP} may result from the decrease in mobility that occurs due to the silane crosslinking (see Sec. 3.5), making the aggregation of the polymers less favorable upon repeated cycling. The decrease in favorability of structure aggregation is supported by the increase in T_{Cl} and w_C with cycling. T_{Cl} increases to a greater extent than T_{CP}, indicating that the transition broadening occurs due to earlier onset transmission recovery during cooling. Osváth and Iván report that upon cooling aqueous PNIPAM, breakup of aggregates and polymer/polmyer H-bonding occurs at higher temperatures (earlier in the transition) than chain re-solvation.[46] Therefore, the earlier onset recovery of transmittance likely results from the breakup of H-bonding between aggregates. While the chains within each structure are likely dense above T_{CP}, the interactions between individual structures are reduced, leading to an earlier onset to the aggregate breakup. During the cooling cycles for $N_{293}[N_{143}/T_8]$, the low temperature transmittance behavior is similar between cycles; thus, the transition primarily broadens at high temperatures during the beginning of cooling, resulting from the reduced inter-aggregate in-

teractions. This effect is especially pronounced by normalizing each individual temperature ramp, highlighting the similarities in the low T optical response (Fig. S80). The small structures formed in $N_{293}[N_{143}/T_8]$ and $N_{283}[N_{113}/T_8]$ (Fig. 6) may lead to this earlier onset in optical clearing, as a smaller portion of the aggregates are of a sufficient size to scatter light compared to polymers that form larger structures, minimizing the aggregate breakup needed to increase transmittance.

In summary, blocky-functionalized copolymers exhibit near-complete transmittance recovery at low temperatures after thermal cycling, though higher TMA content copolymers retain a blue hue. While light silane coupling prevents complete recovery, the large PNIPAM blocks enable chain rehydration below T_{Cl}, causing aggregate breakup and substantial transmission recovery. In contrast, TMA randomly distributed along the chain reduces the length of pure PNIPAM segments in N_{400}/T_{14}, more effectively restricting polymer mobility and swelling once crosslinks are formed. Even if the chains are able to hydrate below T_{Cl}, crosslinks between chains and aggregates can prevent structure breakup, leading to permanent opacity. In contrast, the blocky-functionalized copolymers display repeated cyclability, potentially resulting from the large PNIPAM domains covering the surface of the structures above T_{CP} after the first cycle, serving as a physical barrier to inter-aggregate crosslinking. Thus with cycling, TMA likely continues to crosslink within the structures formed during the first cycle, but the transmittance response is maintained due to minimal coupling between aggregates and the high mobility of the PNIPAM chain ends. The blocky-functionalized polymers have similar trends in the optical transitions with thermal cycling, where the critical temperatures and transitions widths increase, with the greatest increase occurring after the first cycle. These trends suggest the formation of compact structures where inter-aggregate interactions are reduced, as evidenced by the decrease in transmittance drop at high T and the earlier-onset aggregate breakup during cooling. Utilizing blocky-functionalized polymers in applications requiring consistent optical responses over numerous cycles may be advantageous as the effect of continued silane coupling is minimized in comparison to the random copolymers.

3.5 Architectural impacts on chain mobility and recovery through thermal cycling

Variable-temperature ^{1}H NMR (VT-NMR) was used to assess the polymer mobility during thermal cycling by defining an immobilization factor p, which compares the relative integral intensities of protons corresponding to the polymer (Eqn. 2.9); here, p is examined for the four regions of the spectra labelled in Fig. 11. This immobilization factor has been used by Spěváček and coworkers when characterizing the micellization and thermoresponsivity of PNIPAM-containing block copolymers.[67] Here, p corresponds to the fraction of immobilized units; at low T when the polymer is a hydrated coil, $p = 0$. As T increases and the chains begin to collapse, expel solvent, and aggregate, the proton signals decrease, causing p to increase towards a maximum of 1. In Fig. 11 the polymer ^{1}H resonances for $N_{400}T_{14}$ vary in integral intensity with temperature. At high T, small signals are still visible, likely due to the residual bound solvent.[68]

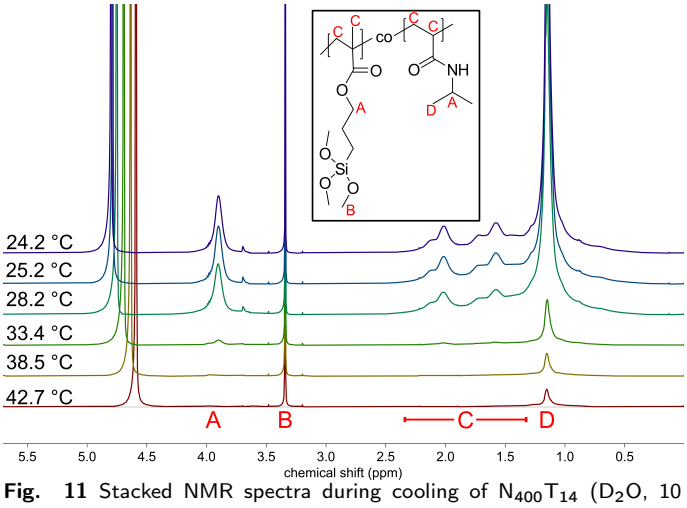

Fig. 11 Stacked NMR spectra during cooling of $N_{400}T_{14}$ (D_2O, 10 mg/mL) demonstrates partial recovery of chain solvation as shown by the intensity increase in peak intensities.

Across polymers, the polymer mobility is high in all regions at low temperatures (<30 °C, Fig. 12). Near the cloud point temperatures (∼34 °C), the chains begin to expel solvent and collapse from hydrated coils to dehydrated globules, increasing p for all protons except those associated with the methoxysilane peak (**B** in Fig. 11). Further increasing the temperature leads to nearly complete chain immobilization ($p \approx 1$). Upon cooling, all samples recover mobility to a degree; however the extent of the recovery and the associated hysteresis depends on TMA content and configuration. Curiously, the integral intensity of the methoxysilane protons does not change appreciably during cycling (**B** in Figs. 11, 12, S83, and S84). The high water content and elevated temperatures likely lead to a rapid hydrolysis of the methoxysilane groups, yielding hydroxy-functionalized silane groups and methanol (see Fig. S81 for reaction mechanism). No change in proton chemical shift is expected as the methoxysilanes are hydrolyzed to methanol (**B** in Fig. 11).[69] If these protons are no longer bound to the polymer, the signal intensity would not be affected by polymer mobility loss, as methanol remains in solution.

The TMA content in random copolymers drastically alters the temperature-dependent immobilization behavior, shown in Fig. 12a-b for $N_{456}T_2$ and $N_{400}T_{14}$, respectively. PNIPAM homopolymers and P(NIPAM-co-TMA) with low TMA incorporation demonstrate complete mobility recovery (p=0) upon cooling with little hysteresis (Figs. 12a, S83a). Although hysteresis behavior of PNIPAM solutions appears in other characterization methods (see Sec. 3.2 and 3.4), this surprising absence of hysteresis in VT-NMR experiments has been reported previously.[67] The hysteresis observed in other characterization methods including CPT and DLS arises from other processes such as aggregate breakup,[46] suggesting that the recovery in chain mobility precedes aggregate breakup and optical clearing. No permanent mobility loss is expected for PNIPAM homopolymer as no intermolecular crosslinking occurs. While N_{456}/T_2 has ∼2 TMA groups per chain that can form crosslinks, any potential crosslinking does not permanently reduce chain mobility. When the TMA content is higher, permanent immobilization is observed (Fig. 12b). In N_{400}/T_{14},

the greater extent of intermolecular crosslinking reduces the ability of chains to separate and rehydrate at lower temperatures, causing a wide hysteresis and incomplete recovery. Taking additional scans at 24 °C upon cooling leads p to decrease slightly but p never returns to zero, indicating permanent structural change (28% irrecoverable mobility).

Blocky-functionalized polymers behave distinctly from the homopolymer and random copolymers, displaying a composition-dependent hysteresis with greater immobilization upon cooling than during heating (Figs. 12c,d, S84). The largest hysteresis for blocky-functionalized polymers is seen for the polymer with the largest B-block (Fig. 12d). Further, the hysteresis in temperature when p=0.5 is strongly correlated with the B-block molecular weight; see Fig. S85 for definition of hysteresis parameters and Fig. S86 for multivariate analysis. Narrower hysteresis occurs in polymers with smaller B-blocks and lower TMA contents (Fig. 12c). The apparent self-assembly and possibility of inter-chain crosslinks at higher TMA contents likely contribute to the hysteresis, by providing an additional barrier for rehydration of PNIPAM segments in the B-block near the core of the aggregate structure. However, nearly complete recovery is observed in all cases, indicating little permanent mobility reduction.

Compared to the random copolymers, the blocky-functionalized copolymers contain long blocks of pure PNIPAM that are not constrained by silane coupling, minimizing the permanent reduction in overall chain mobility after thermal cycling because the crosslinking is limited to smaller chain sections. The B-block TMA fraction for $N_{293}[N_{143}/T_8]$ and $N_{283}[N_{113}/T_8]$ (5.2% mol and 6.6% mol, respectively) is higher than $F_{TMA,AB}$ of the whole N_{400}/T_{14} polymer (3.5% mol), thus ample opportunities are available for crosslinks to form in the B-blocks. However, while $N_{293}[N_{143}/T_8]$ and $N_{283}[N_{113}/T_8]$ have roughly half the TMA units of N_{400}/T_{14}, both blocky-functionalized copolymers exhibit irreversible mobility losses far below ($\sim 1/10^{th}$) that of N_{400}/T_{14}. Interestingly, mobility loss after thermal cycling increases linearly with TMA content; see Fig. S87 for multivariate analysis. However unsurprisingly, the mobility loss per TMA unit is higher for the random copolymers, likely due to the larger fraction of free chain that cannot be constrained by crosslinking in the blocky-functionalized polymers. The free chain end present in the blocky-functionalized polymers is expected to have substantially higher mobility than the random copolymer chains that can be lightly constrained via crosslinking near both chain ends. Additionally, the large domains of pure PNIPAM may provide a barrier to inter-aggregate crosslinking, leading to higher permanent mobility than for a random copolymer with equivalent TMA content.

VT-NMR findings of limited permanent mobility loss for blocky-functionalized polymers corroborate CPT results, where blocky-functionalized polymers demonstrated a high degree of cyclability, even at high TMA content. The near-complete recovery of p closely corresponds to the high transmittance recovery (Fig. 9). The high chain mobility loss across polymers with increasing temperature demonstrates that the chains collapse and dehydrate to similar extents for all samples. Therefore, differences in optical behavior are likely due to factors impacting the aggregate formation, size, and breakup, as previously hypothesized. The hysteresis observed via VT-NMR likely results from the additional barriers for chain re-hydration. In N_{400}/T_{14}, the regular crosslinks formed at elevated temperatures effectively trap parts of the chain in the globular state while also restricting the ability of the chains to reorient and form H-bonds with the solvent. While the blocky-functionalized polymers show higher mobility recovery, the observed hysteresis likely arises for similar reasons. While TMA units are constrained to a portion of the chain, the chains that do form intermolecular crosslinks are immobilized at one chain end, near the center of the aggregate. Therefore, when re-solvating, the chains need to overcome barriers due to physical restriction and from proximity to the hydrophobic TMA groups that discourage re-hydration. Additionally, the blocky-functionalized polymers with higher TMA content form smaller and more uniform structures at elevated temperatures compared to the random copolymers (Sec. 3.2). The density of these structures provides an additional barrier to re-solvation while still allowing for high recovery of mobility at low T. In the cases of $N_{293}[N_{143}/T_8]$ and $N_{283}[N_{113}/T_8]$, the TMA content and localization is sufficient to decrease the aggregate size compared to other samples; however, since the TMA in localized to one chain end, the chain mobility after cycling is not uniformly decreased with inter-chain crosslinking, as can be seen in N_{400}/T_{14}. While the blocky-functionalized polymers display additional barriers to regaining mobility, the free PNIPAM chain ends provide ample conformational freedom to minimize permanent mobility loss.

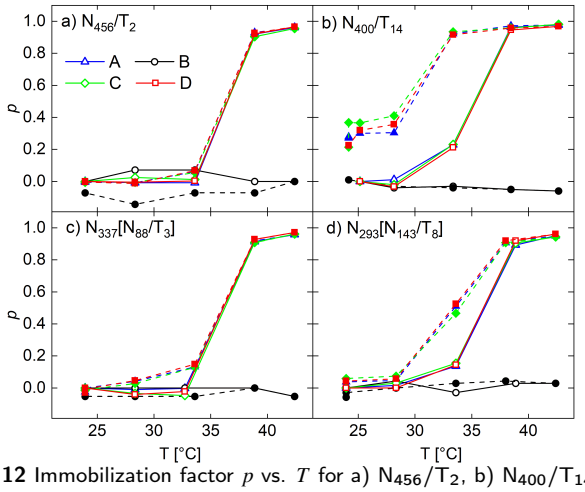

Fig. 12 Immobilization factor p vs. T for a) N_{456}/T_2, b) N_{400}/T_{14}, c) $N_{337}[N_{88}/T_3]$, and d) $N_{293}[N_{143}/T_8]$ upon heating (open symbols) and cooling (closed symbols). Legend corresponds to assignments in Fig. 11.

To further understand the connection between VT-NMR and CPT results, VT-NMR hysteresis was quantified by extracting a difference in temperature at p=0.5 ($dT_{p=0.5}$) and a difference in p at T=34 °C ($dp_{34\,°C}$) (Fig. S85). When compared to the CPT hysteresis during heating, X_H, the values of $dT_{p=0.5}$ are smaller across polymers, influenced in part by the isothermal temperature steps used in VT-NMR, rather than continuous temperature ramps used in CPT. Despite differences in magnitude, these hysteresis parameters are strongly correlated (Fig. S89). While the CPT hysteresis can be attributed to the kinetic barriers of chain solvation and aggregate breakup, minimal hysteresis is observed

in VT-NMR for homopolymer PNIPAM and PNIPAM with low TMA incorporation. Though the optical transition may not be complete at these temperatures due to presence of large aggregates that can scatter light, the chain mobility at this point is similar upon heating and cooling, suggesting similar chain hydration. The observed differences in mobility at 34 °C may also be explained by the CPT transition completeness at the temperature of the NMR scans. For example, $dp_{34\,°C}$ and $T_{Cl,1}$ are negatively correlated (Fig. S88), indicating that the higher the clearing temperature, the more complete the transition will be at 34 °C, minimizing the hysteresis. The lower clearing points and greater hysteresis in polymers with higher TMA content indicate that these polymers have a larger barrier to re-gaining mobility upon cooling.

4 Conclusions

Despite the numerous reports using *N*-isopropyl acrylamide (NIPAM) and 3-(trimethoxysilyl)propyl methacrylate (TMA) to produce macromolecular structures with thermosensitivity, the effects of P(NIPAM-co-TMA) chain architecture on this responsiveness had not been investigated thoroughly. Here, reactive TMA groups copolymerized via RAFT with NIPAM were found to preferentially incorporate into the polymer chain. Polymer architecture and TMA content led to distinct aggregate structures, optical responses, and thermal cyclability. Dynamic light scattering demonstrated that the synthesized random and blocky-functionalized copolymers aggregated into large structures above the cloud point. Smaller, lower dispersity structures were observed for blocky-functionalized copolymers despite a total TMA content of $\leq$2% mol, suggesting assembly of controlled structures due to localized hydrophobic TMA groups. In comparison to PNIPAM homopolymer, TMA-containing copolymers display distinct optical behavior depending on TMA content and chain architecture, with only a few TMA repeat units per chain. In blocky-functionalized copolymers, changes in transmittance over several thermal cycles can be rationalized by TMA-driven structure formation and light silane coupling. Polymers containing more TMA form smaller structures with intra-aggregate crosslinks above T_{CP} which scatter less light; however, polymers with fewer TMA groups form larger, less well-defined structures that lead to lower transmittance above T_{CP}. Random copolymers with a large number of TMA groups show a reduced thermoreversibility with increasing cycle number, indicating that significant silane coupling constrains the motion of the PNIPAM chain. Blocky-functionalized polymers not only demonstrate greater optical recovery upon cycling, but also regain chain mobility upon cooling earlier and more completely than equivalent random copolymers. These findings demonstrate that low TMA incoporation can be used as an effective strategy to control the assembly and thermal cyclability in these inorganic-functionalized responsive polymer solutions, which could potentially be harnessed to create a range of covalently-crosslinked structures and modified surfaces with well-controlled morphology and thermal response.

Author Contributions

L.L. performed cryo-TEM and assisted with interpretation of the micrographs. C.A.P.N. synthesized and characterized EMP, and assisted in interpreting CPT results. J.D.L. performed all other experiments and syntheses and wrote the manuscript. M.A.C. supervised the research and assisted in manuscript writing.

Conflicts of interest

There are no conflicts to declare.

Acknowledgements

Cryo-TEM was carried out in the Characterization Facility, University of Minnesota using support from the Materials Research Facilities Network from the NSF through the MRSEC (Award Number DMR-2011401); the facility also receives support from the NSF through the NNCI (Award Number ECCS-2025124). NMR instruments reported in this publication were supported by the Office of the Vice President of Research, College of Science and Engineering, and the Department of Chemistry at the University of Minnesota. Additional NMR instruments reported in this publication was supported by the Office of the Director, National Institutes of Health, under Award Number S10OD011952. The content is solely the responsibility of the authors and does not necessarily represent the official views of the National Institutes of Health.

Notes and references

1 C.-W. Lee, B.-K. Choi and M.-S. Gong, *Analyst*, 2004, **129**, 651.
2 S. Hajebi, A. Abdollahi, H. Roghani-Mamaqani and M. Salami-Kalajahi, *Langmuir*, 2020, **36**, 2683–2694.
3 J. J. Chung, S. Li, M. M. Stevens, T. K. Georgiou and J. R. Jones, *Chem. Mater.*, 2016, **28**, 6127–6135.
4 W. Li, C.-H. Kuo, I. Kanyo, S. Thanneeru and J. He, *Macromolecules*, 2014, **47**, 5932–5941.
5 A. Pan, L. He, T. Zhang and X. Zhao, *Colloid Polym. Sci.*, 2015, **293**, 2281–2290.
6 M. Ashraful Alam, M. Takafuji and H. Ihara, *J. Colloid Interface Sci.*, 2013, **405**, 109–117.
7 D. Roy, W. L. A. Brooks and B. S. Sumerlin, *Chem. Soc. Rev.*, 2013, **42**, 7214.
8 M. R. Matanović, J. Kristl and P. A. Grabnar, *Int. J. Pharm.*, 2014, **472**, 262–275.
9 S. Brahim, D. Narinesingh and A. Guiseppi-Elie, *Biomacromolecules*, 2003, **4**, 1224–1231.
10 J. Y. Quek, Y. Zhu, P. J. Roth, T. P. Davis and A. B. Lowe, *Macromolecules*, 2013, **46**, 7290–7302.
11 L. Ahmadkhani, M. Abbasian and A. Akbarzadeh, *Des. Monomers Polym.*, 2017, **20**, 406–418.
12 A. E. Smith, X. Xu, S. E. Kirkland-York, D. A. Savin and C. L. McCormick, *Macromolecules*, 2010, **43**, 1210–1217.
13 C. Chang, H. Wei, J. Feng, Z.-C. Wang, X.-J. Wu, D.-Q. Wu, S.-X. Cheng, X.-Z. Zhang and R.-X. Zhuo, *Macromolecules*, 2009, **42**, 4838–4844.
14 M. Kaufmann, Y. Jia, L. Renner, S. Gupta, D. Kuckling, C. Werner and T. Pompe, *Soft Matter*, 2010, **6**, 937.
15 M. Grasinger, *Soft Matter*, 2020, 21.
16 K. Theodosiou, A. Dokouzis, I. Antoniou and G. Leftheriotis, *Sol. Energy Mater Sol. Cells*, 2019, **202**, 110124.

17 Y. Zhou, M. Layani, S. Wang, P. Hu, Y. Ke, S. Magdassi and Y. Long, *Adv. Funct. Mater.*, 2018, **28**, 1705365.

18 D. W. R. Balkenende, *Nat. Commun.*, 2016, **7**, 9.

19 G. L. Fiore, S. J. Rowan and C. Weder, *Chem. Soc. Rev.*, 2013, **42**, 7278.

20 Y. Huang, A. M. Jazani, E. P. Howell, J. K. Oh and M. G. Moffitt, *ACS Appl. Mater. Interfaces*, 2020, 14.

21 M.-M. Xu, R.-J. Liu and Q. Yan, *Chinese J. Polym. Sci.*, 2018, 19.

22 M. A. C. Stuart, W. T. S. Huck, J. Genzer, M. Müller, C. Ober, M. Stamm, G. B. Sukhorukov, I. Szleifer, V. V. Tsukruk, M. Urban, F. Winnik, S. Zauscher, I. Luzinov and S. Minko, *Nature Mater.*, 2010, **9**, 101–113.

23 H. Wei, C. Cheng, C. Chang, W.-Q. Chen, S.-X. Cheng, X.-Z. Zhang and R.-X. Zhuo, *Langmuir*, 2008, **24**, 4564–4570.

24 C. Chang, H. Dan, L.-P. Zhang, M.-X. Chang, Y.-F. Sheng, G.-H. Zheng and X.-Z. Zhang, *J. Appl. Polym. Sci.*, 2015, 11.

25 Z. Osváth, T. Tóth and B. Iván, *Macromol. Rapid Commun.*, 2017, **38**, 1600724.

26 C.-W. Lee, H.-S. Park, J.-G. Kim and M.-S. Gong, *Macromol. Res.*, 2005, **13**, 96–101.

27 Z. Yao and M. Yang, *Sens. Actuators B Chem.*, 2006, **117**, 93–98.

28 L. Jin, C.-H. Liu, D. Cintron, Q. Luo, M.-P. Nieh and J. He, *Langmuir*, 2021, **37**, 9865–9872.

29 M. Cao, Y. Wang, X. Hu, H. Gong, R. Li, H. Cox, J. Zhang, T. A. Waigh, H. Xu and J. R. Lu, *Biomacromolecules*, 2019, **20**, 3601–3610.

30 C. Chang, H. Wei, Q. Li, B. Yang, N. Chen, J.-P. Zhou, X.-Z. Zhang and R.-X. Zhuo, *Polym. Chem.*, 2011, **2**, 923.

31 F.-W. Wang, C.-W. Hsu and C.-C. Hsieh, *ACS Appl. Mater. Interfaces*, 2019, **11**, 8591–8600.

32 M. E. Alf, A. Asatekin, M. C. Barr, S. H. Baxamusa, H. Chelawat, G. Ozaydin-Ince, C. D. Petruczok, R. Sreenivasan, W. E. Tenhaeff, N. J. Trujillo, S. Vaddiraju, J. Xu and K. K. Gleason, *Adv. Mater.*, 2009, **22**, 1993–2027.

33 S. Li, E. N. Davis, X. Huang, B. Song, R. Peltzman, D. M. Sims, Q. Lin and Q. Wang, *J. Diabetes Sci. Technol.*, 2011, **5**, 1060–1067.

34 S. Fujishige, K. Kubota and I. Ando, *J. Phys. Chem.*, 1989, **93**, 3311–3313.

35 T. E. de Oliveira, C. M. Marques and P. A. Netz, *Phys. Chem. Chem. Phys.*, 2018, **20**, 10100–10107.

36 C. Wu and X. Wang, *Phys. Rev. Lett.*, 1998, **80**, 4092–4094.

37 M. J. A. Hore, B. Hammouda, Y. Li and H. Cheng, *Macromolecules*, 2013, **46**, 7894–7901.

38 F. M. Winnik, H. Ringsdorf and J. Venzmer, *Macromolecules*, 1990, **23**, 2415–2416.

39 W. Xiong, X. Gao, Y. Zhao, H. Xu and X. Yang, *Colloids Surf. B*, 2011, **84**, 103–110.

40 H. Wu, D. Dwight and N. Huff, *Compos. Sci. Technol.*, 1997, **57**, 975–983.

41 M. Masmoudi, C. Rahal, M. Abdelmouleh and R. Abdelhedi, *Appl. Surf. Sci.*, 2013, **286**, 71–77.

42 C.-H. Ko, C. Henschel, G. P. Meledam, M. A. Schroer, R. Guo, L. Gaetani, P. Müller-Buschbaum, A. Laschewsky and C. M. Papadakis, *Macromolecules*, 2021, **54**, 5825–5837.

43 Q. Zhang, P. Schattling, P. Theato and R. Hoogenboom, *Polym. Chem.*, 2012, **3**, 1418.

44 X. Lang, A. D. Patrick, B. Hammouda and M. J. A. Hore, *Polymer*, 2018, **145**, 137–147.

45 H. Ren, X.-P. Qiu, Y. Shi, P. Yang and F. M. Winnik, *Macromolecules*, 2020, **53**, 5105–5115.

46 Z. Osváth and B. Iván, *Macromol. Chem. Phys.*, 2017, **218**, 1600470.

47 S. Darvishmanesh, X. Qian and S. R. Wickramasinghe, *Curr. Opin. Chem. Eng.*, 2015, **8**, 98–104.

48 S. K. Kang, D. H. Ho, C. H. Lee, H. S. Lim and J. H. Cho, *ACS Appl. Mater. Interfaces*, 2020, **12**, 33838–33845.

49 W. Wang, X. Hao, S. Chen, Z. Yang, C. Wang, R. Yan, X. Zhang, H. Liu, Q. Shao and Z. Guo, *Polymer*, 2018, **158**, 223–230.

50 W. Yang and F. Zhou, *Biosurface Biotribology*, 2017, **3**, 97–114.

51 Z. Osváth, T. Tóth and B. Iván, *Polymer*, 2017, **108**, 395–399.

52 Z. Cao, B. Du, T. Chen, H. Li, J. Xu and Z. Fan, *Langmuir*, 2008, **24**, 5543–5551.

53 J. Wu, W. Zhai, X. Gao, B. Liu, R. Zhang and Y. Yu, *Polym. Bull.*, 2021, **78**, 753–768.

54 V. Mellon, D. Rinaldi, E. Bourgeat-Lami and F. D'Agosto, *Macromolecules*, 2005, **38**, 1591–1598.

55 A. L. B. Maçon, S. L. Greasley, C. R. Becer and J. R. Jones, *Macromol. Rapid Commun.*, 2015, **36**, 2060–2064.

56 B. V. K. J. Schmidt, M. Hetzer, H. Ritter and C. Barner-Kowollik, *Macromolecules*, 2011, **44**, 7220–7232.

57 M. Fineman and S. D. Ross, *J. Polym. Sci.*, 1950, **5**, 259–262.

58 T. Kelen, F. Tüdős and B. Turcsányi, *Polym. Bull.*, 1980, **2**, 71–76.

59 A. L. Holmberg, M. G. Karavolias and T. H. Epps, *Polym. Chem.*, 2015, **6**, 5728–5739.

60 G. G. Odian, *Principles of polymerization*, Wiley-Interscience, Hoboken, N.J, 4th edn, 2004.

61 J. J. Benvenuta-Tapia, J. A. Tenorio-López and E. Vivaldo-Lima, *Macromol. React. Eng.*, 2018, **12**, 1800003.

62 F. Zeng, Z. Tong and H. Feng, *Polymer*, 1997, **38**, 5539–5544.

63 J. Liu, R. Pelton and A. N. Hrymak, *J. Colloid Interface Sci.*, 2000, **227**, 408–411.

64 S. Fujishige, *Polym. J.*, 1987, **19**, 297–300.

65 Y. Ding, X. Ye and G. Zhang, *Macromolecules*, 2005, **38**, 904–908.

66 D. Neibloom, M. A. Bevan and J. Frechette, *Langmuir*, 2021, **37**, 11625–11636.

67 J. Spěváček, R. Konefał, J. Dybal, E. Čadová and J. Kovářová, *Eur. Polym. J.*, 2017, **94**, 471–483.

68 Y. Maeda, T. Higuchi and I. Ikeda, *Langmuir*, 2000, **16**, 7503–7509.

69 H. E. Gottlieb, V. Kotlyar and A. Nudelman, *J. Org. Chem.*, 1997, **62**, 7512–7515.